

Inversion Ring in Chromonic Twisted Hedgehogs: Theory and Experiment

Federica Ciuchi* and Maria Penelope De Santo†
CNR-Nanotec c/o Physics Department, University of Calabria,
Ponte Bucci, Cubo 31C, 87036 Arcavacata di Rende, Italy

Silvia Paparini‡
Department of Mathematics, University of Pavia, Via Ferrata 5, 27100 Pavia, Italy

Lorenza Spina§
CNR-Nanotec c/o Physics Department, University of Calabria,
Ponte Bucci, Cubo 31C, 87036 Arcavacata di Rende, Italy and
Physics Department, University of Calabria, Ponte Bucci cubo 33B, Arcavacata di Rende 87036, CS, Italy

Epifanio G. Virga¶
Department of Mathematics, University of Pavia, Via Ferrata 5, 27100 Pavia, Italy
(Dated: January 8, 2024)

Twisted hedgehogs are defects in spherical cavities with homeotropic anchoring for the nematic director that arise when twist distortions are sufficiently less energetic than splay (and bend) distortions. They bear a characteristic *inversion ring*, where the director texture changes the sense it spirals about the center of the cavity. This paper applies a quartic twist theory recently proposed to describe the elasticity of chromonics to explain a series of inversion rings observed in aqueous solutions of SSY at two different concentrations. The theory features a phenomenological length a , whose measure is extracted from the data and shown to be fairly independent of the cavity radius, as expected for a material constant.

I. INTRODUCTION

Among the many lyotropic phases, chromonic liquid crystals (CLCs) have attracted attention for their potential applications in life sciences [1–4]. These materials are constituted by plank-shaped molecules that arrange themselves in stacks when dissolved in (usually aqueous) solution. For sufficiently large concentrations or small temperatures, the constituting stacks give rise to an ordered phase, either nematic or columnar [5–9]. Here, we shall only be concerned with the nematic phase. Numerous substances have a CLC phase; these include organic dyes (especially those common in food industry), drugs, and oligonucleotides.

The classical elastic Oseen-Frank theory has been applied to CLCs, but the twist constant K_{22} has to be taken anomalously small to explain the spontaneous *double* twist exhibited by these materials when confined to cylindrical cavities with degenerate planar anchoring on the lateral boundary [10, 11]. In particular, K_{22} must be smaller than the saddle-splay constant K_{24} , thus violating one of the inequalities Ericksen [12] had put forward to guarantee that the Oseen-Frank stored energy be bounded below. However, as shown in [13], free-boundary problems may reveal paradoxical consequences stemming from violating Ericksen’s inequalities. If $K_{22} < K_{24}$, a CLC droplet in an isotropic fluid enforcing degenerate planar anchoring, is predicted to be unstable against *shape* perturbations: it would split indefinitely in smaller droplets, while the total free energy plummets to negative infinity [13]. This prediction is in sharp contrast with the wealth of experimental observations of CLC tactoids in the biphasic region, where nematic and isotropic phases coexist in equilibrium [14–18].

To resolve this contradiction, a minimalist quartic theory for CLCs was proposed in [19], which adds to the Oseen-Frank energy density a single quartic term in the twist measure; hence the name *quartic twist* theory. It was shown in [19] that indeed within this theory the total free energy of chromonic droplets subject to degenerate planar interfacial anchoring remains bounded below, even if $K_{22} < K_{24}$.

In [20], the quartic twist theory was applied to explain the formation of *inversion rings* within spherical cavities enclosing water solutions of SSY (Sunset Yellow, a dye used in industrially processed food) subject to *homeotropic*

* federica.ciuchi@cnr.it
† maria.desanto@fis.unical.it
‡ silvia.paparini@unipv.it
§ lorospina2@gmail.com
¶ eg.virga@unipv.it

boundary conditions for the director field \mathbf{n} . The predictions of the theory were contrasted with some experimental evidence found in recent literature [21].

Although the comparison was encouraging, it was neither systematic nor self-consistent: it was based on a single example and used an estimate for a phenomenological length a featuring in the theory that came from a different experiment. Thus, the motivation for the present study is to provide a systematic and self-consistent validation of the quartic twist theory.

We observed a large number of microcavities enclosing a SSY solution at two distinct concentrations and three different times since the samples were prepared. We extracted the length a in different physical conditions from direct measurements of the inversion ring.

The paper is organized as follows. In Section II, we summarize the quartic twist theory to make our development self-contained. In Section III, we describe the materials and the experimental methods. Section IV is devoted to the comparison of the experimental data with the proposed theory. Here we extract a and study its dependence on concentration and other factors that may change the physical conditions of the samples as time elapses since their preparation. Finally, in Section V, we collect the conclusions reached in this study. The paper is closed by two Appendices: in one, we disaggregate the data that in the main text were presented in a single universal graph; in the other, we delve in some statistical details that could have hampered our presentation in the body of the paper.

II. QUARTIC TWIST THEORY

In this study we adopt an elastic theory for CLCs that has already been developed and applied in a number of papers [19, 20, 22]. In Section IV, we shall employ it to interpret the experiments described in Section III.

The elastic free energy density that was posited in [19] has the distinguished feature of envisioning a *double twist* (with two equivalent chiral variants) as ground state of CLCs in three-dimensional space. Here we briefly elaborate on this concept.

First, we introduce the independent scalar *measures of distortion* (S, T, B, q) for a director field \mathbf{n} ; they are defined as follows: $S := \text{div } \mathbf{n}$ is the *splay*, $T := \mathbf{n} \cdot \text{curl } \mathbf{n}$ is the *twist*, $B := |\mathbf{b}|$ is the modulus of the *bend* vector $\mathbf{b} := \mathbf{n} \times \text{curl } \mathbf{n}$, and $q > 0$ is the *octupolar splay* [23], derived from

$$2q^2 = \text{tr}(\nabla \mathbf{n})^2 + \frac{1}{2}T^2 - \frac{1}{2}S^2. \quad (1)$$

Then, following a terminology proposed by Selinger [24] (see also [25]), we call *double twist* a distortion characterized by having *all* measures of distortion equal to zero, *but* a single one, T . Somehow ironically, a *single twist* is characterized by having *two* non-zero measures of distortion related to one another:

$$S = 0, \quad B = 0, \quad T = \pm 2q. \quad (2)$$

A single twist is nothing but what others would call a *cholesteric twist*. While a single twist can fill *uniformly* the whole space [26], a double twist cannot. The latter can only be realized locally, not globally: it is thus a *frustrated* ground state. It was shown in [27] that a double twist can, for example, be attained exactly on the symmetry axis of cylinders enforcing degenerate planar anchoring on their lateral boundary.

The simplest way to induce locally a double twist is to add a *quartic twist* term to the classical Oseen-Frank stored energy density [28, 29] and define [19]

$$W_{\text{QT}}(\mathbf{n}, \nabla \mathbf{n}) := \frac{1}{2}(K_{11} - K_{24})S^2 + \frac{1}{2}(K_{22} - K_{24})T^2 + \frac{1}{2}K_{33}B^2 + \frac{1}{2}K_{24}(2q)^2 + \frac{1}{4}K_{22}a^2T^4, \quad (3)$$

where K_{11} is the *splay* constant, K_{22} is the *twist* constant, K_{33} is the *bend* constant, K_{24} the *saddle-splay* constant, and a is a *characteristic length*. W_{QT} is bounded below whenever

$$K_{11} \geq K_{24} \geq 0, \quad (4a)$$

$$K_{24} \geq K_{22} \geq 0, \quad (4b)$$

$$K_{33} \geq 0, \quad (4c)$$

which in this theory replace the celebrated *Ericksen inequalities* [12]. When, as we shall assume here, inequalities (4) hold strictly, W_{QT} is minimum at the *degenerate* double twist characterized by

$$S = 0, \quad T = \pm T_0, \quad B = 0, \quad q = 0, \quad (5)$$

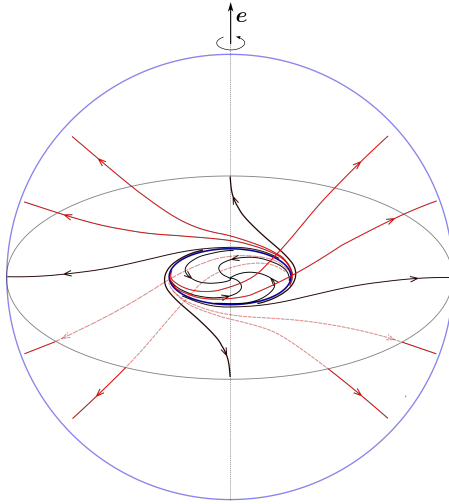


Figure 1: Field lines of \mathbf{n}_T in (8) in a spherical cavity enforcing homeotropic boundary conditions. An inversion ring, depicted in blue, is present on the equatorial plane (orthogonal to the symmetry axis \mathbf{e}). Black lines are field lines lying on the equatorial plane; red lines are field lines coming out of the equatorial plane. The whole 3D picture is obtained by rotating this drawing about \mathbf{e} . This sketch is adapted from Fig. 2 of [20]; it represents only one chiral variant of twisted hedgehog, the other is obtained by reversing the sign of α in (8).

where

$$T_0 := \frac{1}{a} \sqrt{\frac{K_{24} - K_{22}}{K_{22}}}. \quad (6)$$

Here, we shall treat a as a phenomenological parameter to be determined experimentally. We designate the elastic theory based on W_{QT} in (3) as quartic *twist* theory, as among all possible quartic invariant terms in $\nabla\mathbf{n}$ we only consider the one proportional to T^4 (see also [26] for other possible quartic elastic theories).

A. Twisted Hedgehog

The quartic twist theory was applied in [20] to describe the *twisted hedgehog* that forms within a spherical cavity enforcing homeotropic alignment on its boundary. It is known since the seminal work of Lavrentovich and Terentiev [30] that for a splay constant K_{11} sufficiently larger than the twist constant K_{22} , the *radial* hedgehog becomes unstable and acquires a twisted texture (with either sign of chirality equally likely to emerge), see Fig. 1. More precisely, as proved in [31–33], the radial hedgehog loses local stability whenever

$$K_{11} > K_{22} + \frac{1}{8}K_{33}. \quad (7)$$

The original proof of this inequality was given for the Oseen-Frank elastic theory; however, it also applies to the theory associated with the energy density in (3), as both theories share the same second variation of the energy functional [27]. For CLCs, inequality (7) holds because K_{11} and K_{33} are customarily comparable, whereas K_{22} is much smaller (nearly by an order of magnitude).

The field lines shown in Fig. 1 were obtained in [20] by minimizing the total elastic free energy on the trial family of fields defined as

$$\mathbf{n}_T(\mathbf{x}) := \mathbf{R}(\alpha(r)) \frac{\mathbf{x}}{r}, \quad (8)$$

where \mathbf{x} is the position vector, $r := |\mathbf{x}|$, and $\mathbf{R}(\alpha)$ denotes the rotation of angle α about a symmetry axis \mathbf{e} . Letting α depend only on r , we reduced the total elastic free energy to an admittedly complicated functional $\mathcal{F}[\alpha]$ of a single scalar function $\alpha(\rho)$, where $\rho := r/R$ is the only space variable scaled to the radius R of the spherical cavity. \mathcal{F} is even, and so the same energy is assigned to a function α and its opposite. This degeneracy means that minimizers come in pairs of twisted hedgehogs with opposite chirality; Fig. 1 represents only one chiral variant. Three dimensionless parameters feature in \mathcal{F} : the reduced elastic constants $k_1 := K_{11}/K_{22}$ and $k_3 := K_{33}/K_{22}$, and the ratio $\lambda := a/R$.

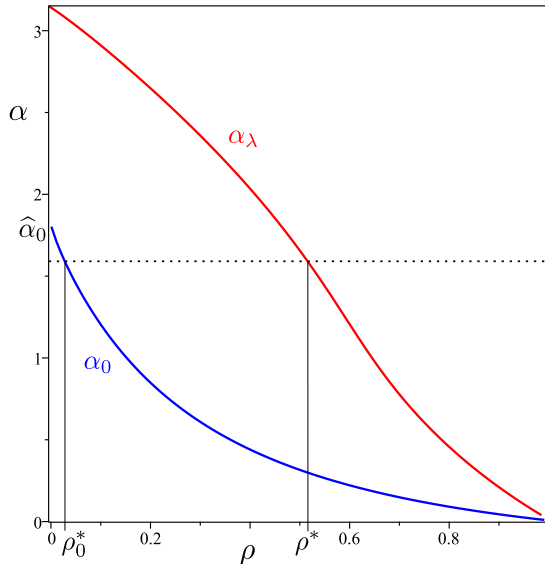


Figure 2: The elastic free energy (positive) minimizer α_λ for reduced elastic constants $k_1 = 7.5$, $k_3 = 9.0$ (which apply to a SSY solution at concentration $c = 30$ wt%), and $\lambda = 0.94$ is compared with the minimizer α_0 according to the Oseen-Frank theory. The dotted line is drawn at $\alpha = \frac{\pi}{2}$; its intercepts with the graphs of α_λ and α_0 designate the (scaled) radii of the inversion ring, $\rho^* := r^*/R \doteq 0.52$ and $\rho_0^* := r_0^*/R \doteq 0.03$, respectively. As shown in [20], $\hat{\alpha}_0 = \arccos(-1/4)$ is the value of α_0 at $\rho = 0$, whereas $\alpha_\lambda(0) = \pi$.

In the special case where $\lambda = 0$, the quartic twist theory reduces to the classical Oseen-Frank theory. Figure 2 shows a typical positive minimizer α_λ of $\mathcal{F}[\alpha]$ compared with the minimizer α_0 of the classical theory.

A remarkable feature of the twisted hedgehog is the *inversion ring* that the nematic director field \mathbf{n} exhibits on the plane orthogonal to the symmetry axis of the distortion texture. There, the direction of winding of the spiralling field lines of \mathbf{n} changes; it has the optical appearance of a disclination (see also Fig. 6 below), but it is *not* a defect, as \mathbf{n} is continuous there.

How the radius r^* of the inversion ring depends on λ was studied in [20]. For given λ , r^* can be read off from Fig. 2: it falls where the graph of α_λ intersects the line $\alpha = \frac{\pi}{2}$. The comparison between α_λ and α_0 suggests that the quartic twist theory may predict inversion rings appreciably larger than those compatible with the Oseen-Frank theory. Figure 3 represents the graph of $\rho^* := r^*/R$ against λ for the same choice of reduced elastic constants made in Fig. 2.

It is the aim of this paper to provide an experimental validation of the theory recalled in this section. This will be achieved by extracting measures of the radius of the inversion ring produced in a number of spherical cavities trapping a solution of Sunset yellow (SSY) in water inside a polymeric matrix enforcing homeotropic anchoring on the nematic director. How these cavities are obtained and with what materials is explained in the following section.

III. EXPERIMENTAL

The material SSY, whose molecular structure is shown in Fig. 4a, was purchased from Sigma-Aldrich and used without further purification. The brute formula is $C_{16}H_{10}N_2Na_2O_7S_2$ and the molecular weight is 452.37.

When dissolved in water it stacks in cylinder formations, the length of which depends on temperature and concentration; the cylinders then give rise to a nematic phase. At room temperature, the nematic phase exists between ca. 28-34 wt% (Fig. 4b), [34].

SSY emulsions were prepared using polydimethylsiloxane (PDMS) as an immiscible matrix (Sylgard, kit 184). PDMS is a liquid polymer that appears oily and transparent and has a high viscosity [21]. To obtain a homeotropic anchoring at the interface, PDMS was used pure, as an oil in which to disperse the liquid crystal solution. PDMS brute formula is $(C_2H_6OSi)_n$, the structure of the repeating unit is shown in Fig. 5.

For the preparation of the chromonic solution, the SSY powder and water were mixed in appropriate proportions to obtain solutions containing SSY 30 wt% and 31.5 wt%. The confinement of chromonic solutions in spherical geometries is achieved by preparing emulsions. The emulsions were prepared by adding a small amount of water-based chromonics solution to the oil matrix (PDMS). By mechanically stirring, a large number of spherical microcavities were obtained.

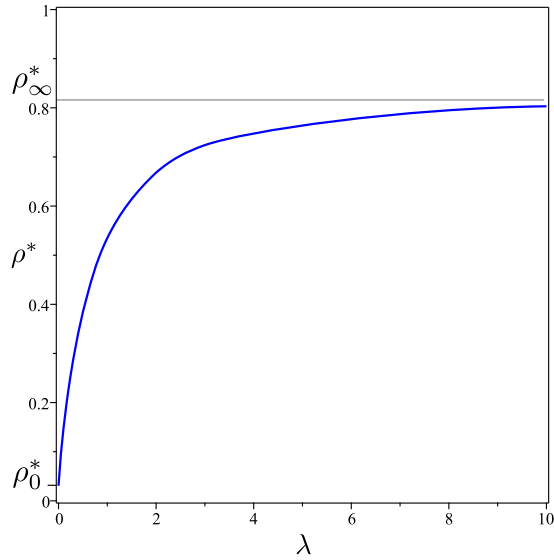
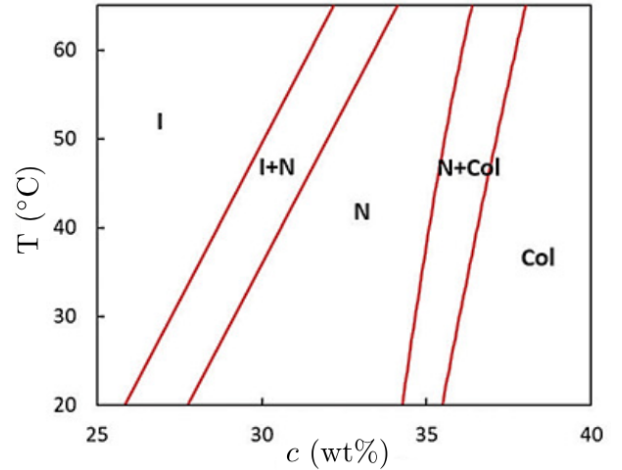
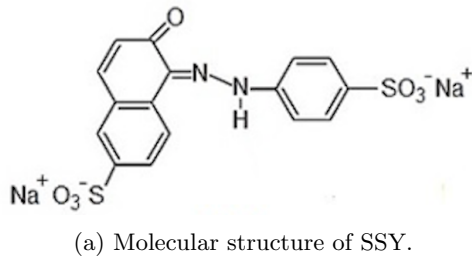


Figure 3: The scaled radius $\rho^* := r^*/R$ of the inversion ring for the elastic free energy minimizer α_λ is plotted against $\lambda := a/R$ for the same reduced elastic constants chosen in Fig. 2. The graph saturates at $\rho_\infty^* \doteq 0.82$, while $\rho_0^* \doteq 0.03$ is the limiting value as $\lambda \rightarrow 0$.



(b) SSY phase diagram.

Figure 4

For microcavity texture investigations, a small amount of the prepared emulsion was sandwiched between two laboratory glass slides separated by mylar stripes of $190\mu\text{m}$. Due to the high viscosity of PDMS, it was not necessary to seal the cell with tape or glue. Microsphere textures were studied using a polarized light microscope (Zeiss Axiolab 5, Axiocam 208 colour). Images were acquired with a monochromatic red filter whose transmission spectrum has peak at 639 nm (with full width at half maximum equal to 10 nm).

IV. COMPARISON WITH THEORY

A typical example of microcavities produced via the method described in Section III is shown in Figure 6. These enclose a SSY solution in water at concentration $c = 30\text{ wt}\%$ and temperature $T = 25^\circ\text{C}$. A similar experiment was also performed with a solution at $c = 31.5\text{ wt}\%$ and same temperature. We conventionally refer to these as Experiment I and II, respectively. In both experiments, observations of the samples at the optical microscope were made immediately after having prepared the cell, as well as one and two days after. These are referred to as Observation

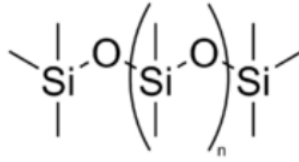


Figure 5: Molecular structure of PDMS.

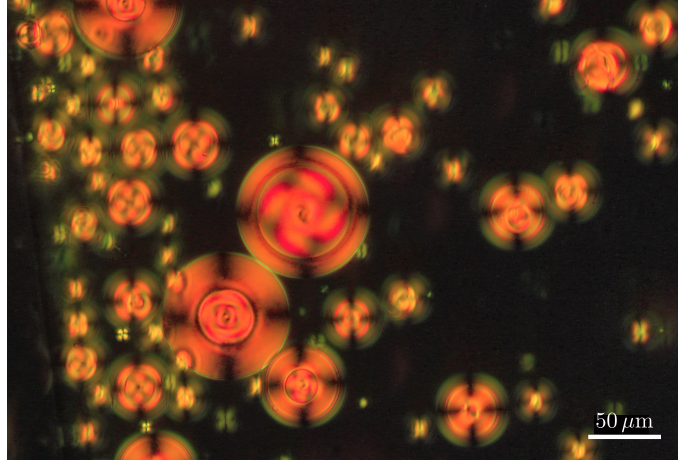


Figure 6: Microcavities enclosing a solution of SSY in water at concentration $c = 30$ wt% and temperature $T = 25$ °C. This particular sample was observed two days after preparation. All cavities allegedly host the same twisted hedgehog, but its symmetry axis is differently oriented relative to the observer. For the cavities viewed along the hedgehog's symmetry axis, the inversion ring is easily identified as a circle; it does not look circular for the others, which are viewed askew (see also Fig. 10b).

0, 1, and 2, respectively; cavities seen in one observation are not the same as cavities seen in another.

A. Inversion Ring Statistics

For each cavity that could be clearly discerned in images like the one in Fig. 6, we measured both r^* and R and then we extracted a from the value of $\lambda = a/R$ read off from the graph like that in Fig. 3 corresponding to the elastic constants of the material at the appropriate concentration and temperature. For the physical conditions of Experiment I, the reduced elastic constants are $k_1 \approx 7.5$ and $k_3 \approx 9.0$, while for those of Experiment II they are $k_1 \approx 11.0$ and $k_3 \approx 10.4$. (These values were derived from the measurements reported in [35–37], which we read as follows. Experiment I: $K_{11} \approx 7.6$ pN, $K_{22} \approx 1.02$ pN, $K_{33} \approx 9.2$ pN; Experiment II: $K_{11} \approx 13.8$ pN, $K_{22} \approx 1.25$ pN, $K_{33} \approx 13.0$ pN.)

The data thus collected for r^* , R , and a were more conveniently organized on a universal graph (depending only on k_1 and k_3) that plots the ratio r^*/a against $R/a = 1/\lambda$. This graph is different for each experiment; it is obtained from the graph in Fig. 3 via the transformation

$$\frac{r^*}{a} = \frac{\rho^*}{\lambda}. \quad (9)$$

This changes the function ρ^* plotted in Fig. 3 against λ into a monotonic function that approaches 0 as $R/a \rightarrow 0$ and grows nonlinearly until becoming asymptotically linear for large R/a , $r^*/R \approx \rho_0^*(R/a)$, where ρ_0^* is the (scaled) radius of the inversion ring predicted by the Oseen-Frank theory. The rearranged data are shown in Fig. 7 for both experiments. As also recalled in [20], the classical Oseen-Frank theory predicts an inversion ring whose radius r_0^* is such that the ratio r_0^*/R depends only on the reduced elastic constants; thus, the graphs representing the prediction of the classical theory in both panels of Fig. 7 are straight lines. More precisely, for Experiment I, $r_0^*/R = \rho_0^* \approx 0.03$, while $r_0^*/R = \rho_0^* \approx 0.06$ for Experiment II. It is apparent that for chromonics the Oseen-Frank theory fails to represent

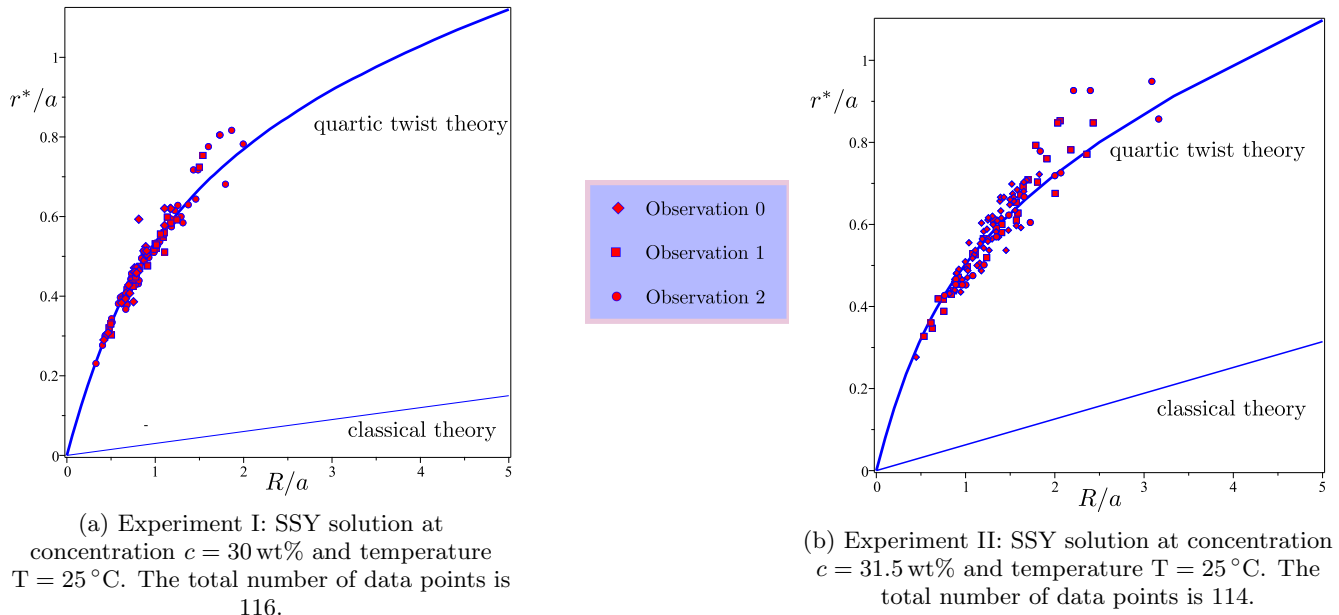


Figure 7: Data collected in all observations. They are shown against the universal graph of the function r^*/a against $R/a = 1/\lambda$ obtained from the function ρ^* plotted in Fig. 3 against λ via the transformation (9). Diamonds refer to samples just prepared (Observation 0), boxes to samples observed after one day (Observation 1), dots to samples observed after two days (Observation 2). Straight lines apply to the classical Oseen-Frank theory; they are recovered asymptotically by the quartic twist theory in the limit as $R/a \rightarrow \infty$.

SSY concentration	Observation 0	Observation 1	Observation 2
30 wt%	$a \approx 47 \mu\text{m}$	$a \approx 41 \mu\text{m}$	$a \approx 33 \mu\text{m}$
31.5 wt%	$a \approx 54 \mu\text{m}$	$a \approx 46 \mu\text{m}$	$a \approx 35 \mu\text{m}$

Table I: Estimates of a for SSY solutions in the physical conditions of different observations.

our data, whereas the proposed quartic twist theory seems in good agreement with both experiments, more so for smaller cavities than for larger ones, for which the inversion ring tends to be larger than predicted by theory.

All collected data are shown in Fig. 7: they include all observations. The reader will find in Appendix A separate illustrations for each observation in both experiments.

Since the measures of both r^* and R are affected by errors, these propagate to a , in a way made possible to estimate by the predicted dependence of ρ^* on λ (shown in Fig. 3). For each observation, we also estimated how the inferred values of a are distributed compared to the measured values of the radius R . Our goal is to show that the former are less dispersed than the latter, as appropriate for a phenomenological length that should only be related to the material and its physical conditions. The comparison is made easier by the *dispersion* histogram shown in Fig. 8 for a single observation (at a given SSY concentration). For completeness, similar dispersion histograms for all other observations are collected in Appendix B. Despite the noise present in the data, we can be reasonably confident in the material nature of a . Quantitative details on how we determined the error bars in Fig. 8 are also given in Appendix B.

B. Estimates of a

The method illustrated in Section IV A led us to the estimates of a collected in Table I. The corresponding deviations from the mean values (which do not exceed 9%) are recorded in Appendix B, which also documents the much larger dispersion in the data set for R .

It is worth remarking that for SSY in the same physical conditions as in Experiment I, in [19] we had estimated $a \approx 6.4 \mu\text{m}$ from the director field observations of [10] in cylinders with planar degenerate conditions on their lateral boundary. The difference (by nearly one order of magnitude) between this estimate and those summarized in Table I might result from the different experimental settings. By the disparity in the number of data collected here

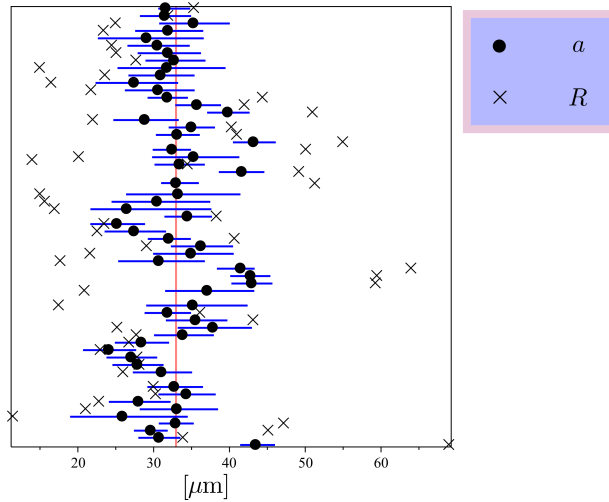


Figure 8: Dispersion histogram of the data in Fig. 7a for the observation two days after preparation in Experiment I. The measured values R_i of the radius R are black crosses and the estimated values a_i of the characteristic length a are black dots (with corresponding blue error bars). The red vertical line marks the mean value $\bar{a} \approx 33 \mu\text{m}$ of a .

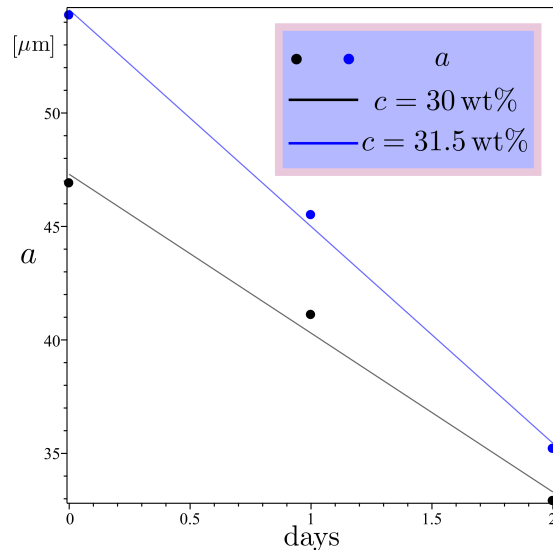


Figure 9: Estimated values of a plotted against the time elapsed since cell preparation for both SSY concentrations, namely, $c = 30 \text{ wt}\%$ (black line) and $c = 31.5 \text{ wt}\%$ (blue line). Dots mark the values in Table I; straight lines are guides for the eye.

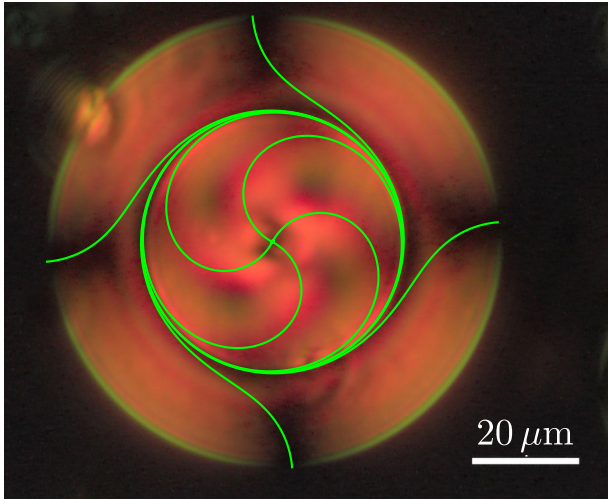
and in [10] and the fact that in [19] we needed to determine two fitting parameters (a and K_{24}) instead of one, we are inclined to think that the estimates summarized in Table I are more reliable.

Two trends emerge clearly from these findings: a increases with concentration and decreases as time elapses since cell preparation (see Fig. 9).

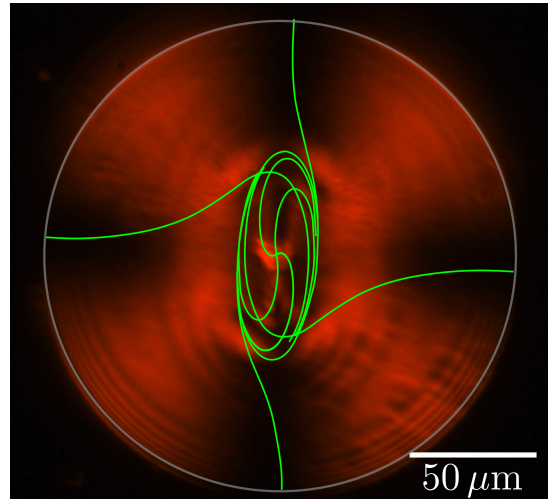
C. Spiralling Cores

As proved in [20] and illustrated in Fig. 1, the quartic twist theory recalled in Section II predicts a distortion *spiralling core* within the inversion ring of a twisted hedgehog. Here we compare with experiment this qualitative feature of the theory.

Among the many observed cavities, we focus on two exemplary cases; they are shown in Fig. 10. In both cases, SSY is at concentration $c = 30 \text{ wt}\%$ and temperature $T = 25 \text{ }^\circ\text{C}$: the cavity in Fig. 10a was observed one day after



(a) Spherical cavity of radius $R \approx 44 \mu\text{m}$ observed after one day from the sample preparation. Taking $a \approx 41 \mu\text{m}$ from Table I, we estimate $r^* \approx 23 \mu\text{m}$.



(b) Spherical cavity of radius $R \approx 105 \mu\text{m}$ observed in a just prepared sample. Taking $a \approx 47 \mu\text{m}$ from Table I, we estimate $r^* \approx 46 \mu\text{m}$.

Figure 10: Spherical cavities enclosing a SSY solution at concentration $c = 30 \text{ wt}\%$ and temperature $T = 25^\circ\text{C}$. The spiralling core predicted by the quartic twist theory (depicted in green) is superimposed to the experimental images. The radius of the inversion ring is estimated by theory (as explained in Section II); its predicted values are in good agreement with direct measures.

preparation, while the cavity in Fig. 10b was observed just at the time of preparation. In the former instance, the spiralling core is observed along the symmetry axis of the twisted hedgehog (at right angles with the plane containing the inversion ring), whereas in the latter it is viewed askew, along a direction that we estimated at the angle $\pi/8$ from the symmetry axis.

Based on this evidence, we may say that the quartic twist theory seems also to be in good qualitative agreement with the experimental observations.

V. CONCLUSIONS

A quartic twist theory for the elasticity of chromonic liquid crystals is subjected to experimental scrutiny. The spiralling texture of twisted hedgehogs in spherical cavities enforcing homeotropic anchoring is characterized by an inversion ring, which can be observed optically. Measurements of the inversion ring are contrasted with both the classical Oseen-Frank theory and the quartic twist theory, and shown to be in better accord with the latter than with the former.

A phenomenological length a features in the proposed theory; it is a material parameter, supposedly depending on both temperature and concentration of the chromonic solution. The data collected for the inversion ring agree with theory if a specific value of a is chosen for each cavity's radius R . The small dispersion in the values of a compared to the dispersion of radii is a testament to the material nature of a , which depends only on the physical conditions in which the observation takes place.

The average of a for each observation is found to increase with concentration and decrease with the time elapsed after sample preparation. The former trend can be understood by recalling that a similar behaviour is shown by the ratio of elastic constants K_{11}/K_{33} in homogeneous chromonic phases (see either Fig. 3 of [35] or Fig. 2c of [37]). According to the microscopic theory developed in [38] (see also [39]) for the elastic properties of liquid crystal phases generated by *flexible* molecules,

$$\frac{K_{11}}{K_{33}} = \frac{\ell}{\delta}, \quad (10)$$

where ℓ is the *contour* length of the constituting molecules and δ is their *persistence* length. In the present context, since δ is far less sensitive to concentration than ℓ , (10) would suggest that ℓ (here the length of CLC aggregates) increases with c . Since a increases with c too, one is led to conjecture that a is an increasing function of ℓ .

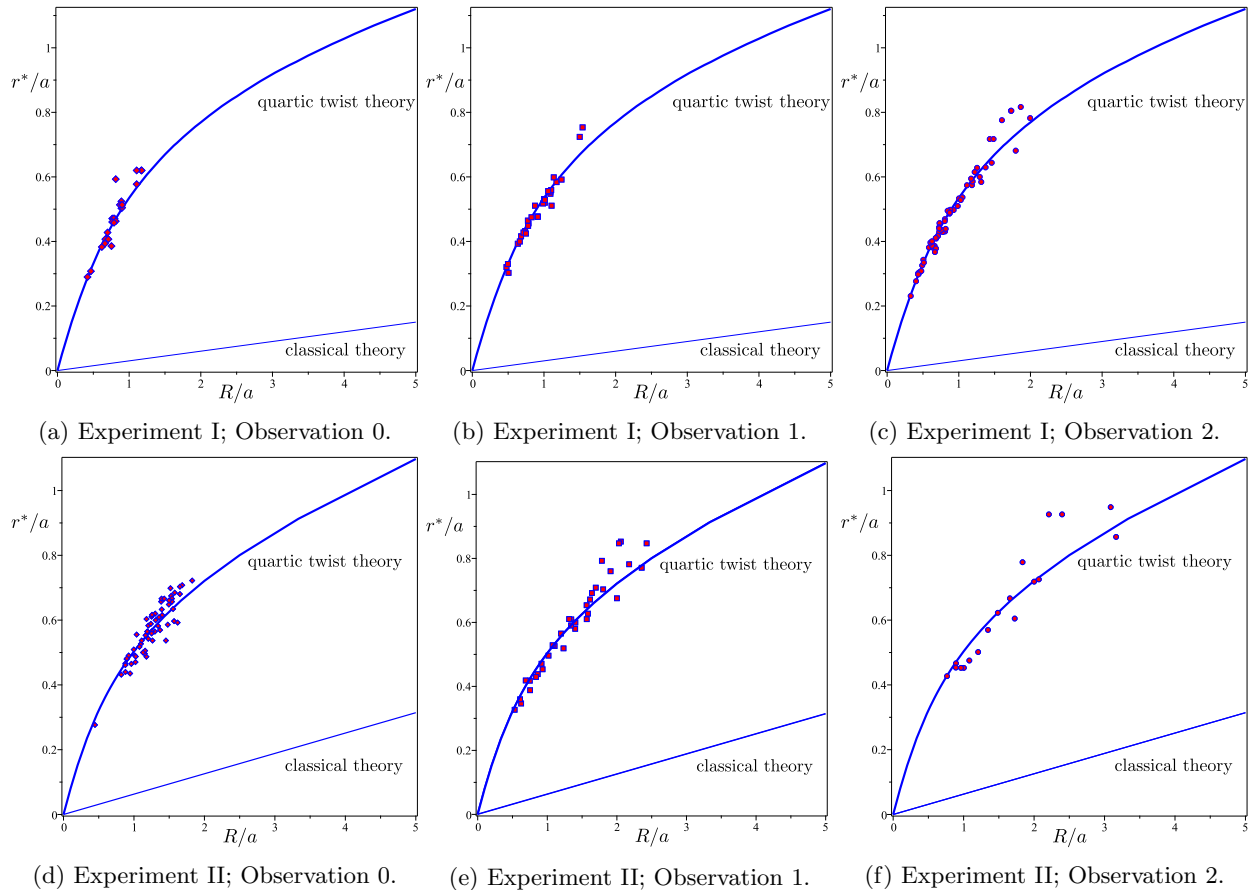


Figure 11: Disaggregation of the data shown in Fig. 7. Experiment I uses a SSY solution at concentration $c = 30$ wt% and temperature $T = 25$ °C; Experiments II uses a SSY solution at concentration $c = 31.5$ wt% and temperature $T = 25$ °C. Observations are denoted 0, 1, or 2, according to whether they took place with the cell just prepared, one, or two days later, respectively.

This is, however, a slippery terrain, as observations of twisted tactoids in the biphasic regime suggested in [17] that ℓ might instead be a decreasing function of c , at least for temperatures just slightly below the biphasic-to-isotropic transition.¹

In our experiments, temperature was not varied, but (different) cavities were observed at different times. The length a was found to decrease as such a *curing* time elapsed. If the conjectured link between a and ℓ is to be trusted, one may interpret this result as suggesting that molecular aggregates become shorter on average (hence larger in number) as the cure progresses. A theoretical validation of this conjecture could be found by building a kinetic model for chromonic molecular aggregation, possibly along lines similar to those that started to be traced in [40, 41].

ACKNOWLEDGMENTS

The UNICAL Group acknowledges financial support through the Italian PRIN 2022 - PNRR Project No. P2022HM5E4 on *Chirality induction in water based self-assembling materials*.

¹ The droplets observed in [17] are in the biphasic region of phase space, where nematic and isotropic phases of the solution coexist in equilibrium, although at different concentrations, higher in the nematic (c_N), lower in the isotropic (c_I); see Fig. 4b. If in [17] $c > c_I$ is the concentration at which the solution is prepared, then the concentration in the twisted tactoids would be $c_N > c$.

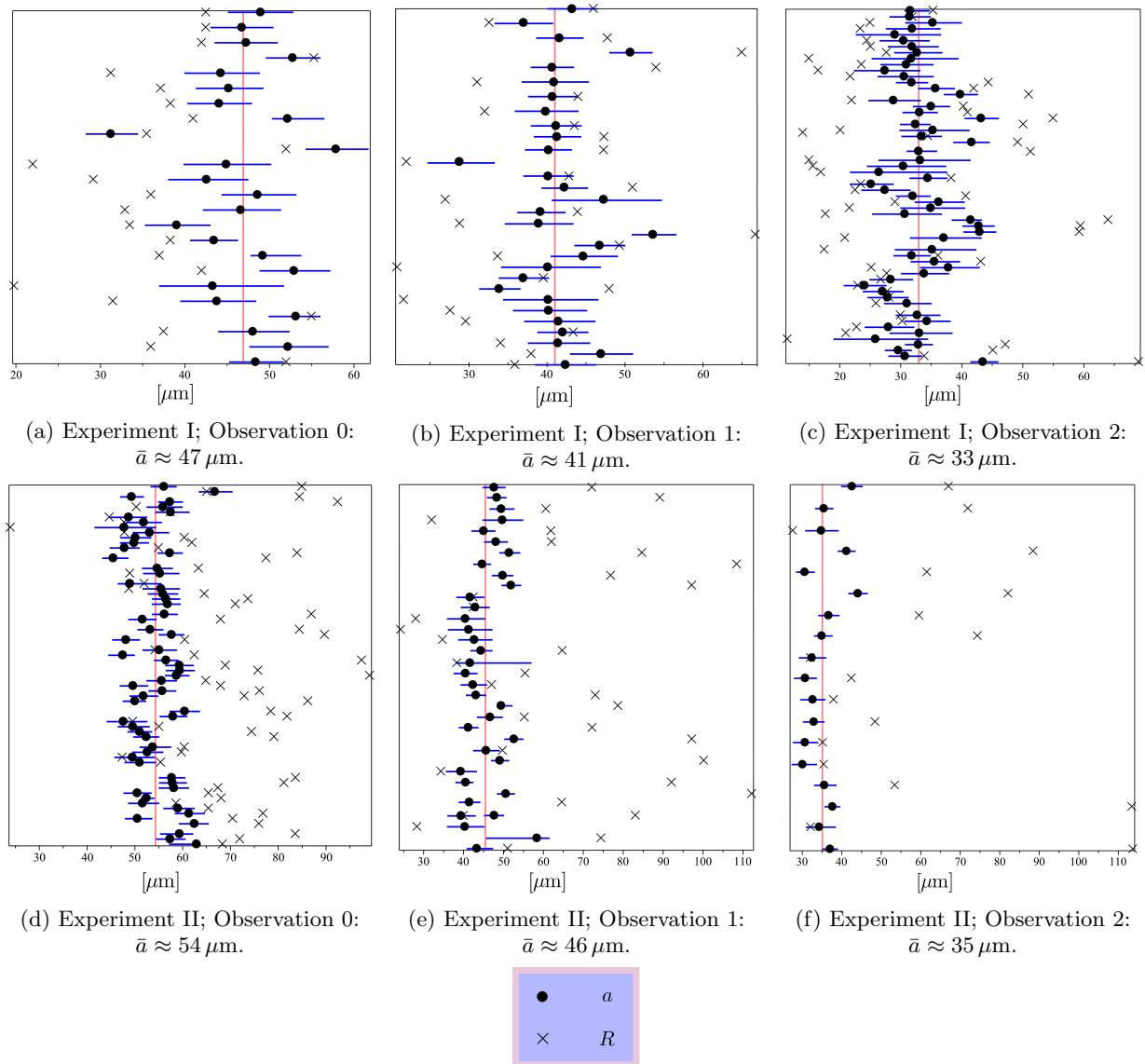


Figure 12: Dispersion histograms comparing the different measures inferred for a to the cavity radii. They are organized according to experiments and observations, precisely as the panels of Fig. 11; in addition, here \bar{a} denotes the average value of a for each set of conditions. All average values are collected in Table I in the main text.

Appendix A: Data Disaggregation

Two distinct experiments were performed and, for each, three observations were made at different times. Experiments, conventionally denoted I and II, used different SSY solutions at room temperature. The data that were aggregated per experiment in Fig. 7 are now disaggregated in Fig. 11.

Appendix B: Error Analysis and Statistical Dispersion

The radii R_i of microcavities and r_i^* of inversion rings were measured on image reproductions; they were all affected by the same absolute error $\Delta R = \Delta r^* = 1 \mu\text{m}$. As a consequence, the corresponding values of $\rho^* = r^*/R$ were listed as $\rho_i^* \pm \Delta\rho_i^*$, where

$$\Delta\rho_i^* := \frac{r_i^*}{R_i} \left(\frac{1}{r_i^*} - \frac{1}{R_i} \right) \Delta r^*. \quad (\text{B1})$$

Experiment	Observation 0	Observation 1	Observation 2
I	$\bar{a} \approx 47 \mu\text{m}$, $\bar{R} \approx 38 \mu\text{m}$ $\mathcal{M}(a) \approx 8\%$, $\mathcal{M}(R) \approx 20\%$	$\bar{a} \approx 41 \mu\text{m}$, $\bar{R} \approx 40 \mu\text{m}$ $\mathcal{M}(a) \approx 8\%$, $\mathcal{M}(R) \approx 24\%$	$\bar{a} \approx 33 \mu\text{m}$, $\bar{R} \approx 32 \mu\text{m}$ $\mathcal{M}(a) \approx 9\%$, $\mathcal{M}(R) \approx 39\%$
II	$\bar{a} \approx 54 \mu\text{m}$, $\bar{R} \approx 68 \mu\text{m}$ $\mathcal{M}(a) \approx 7\%$, $\mathcal{M}(R) \approx 17\%$	$\bar{a} \approx 46 \mu\text{m}$, $\bar{R} \approx 64 \mu\text{m}$ $\mathcal{M}(a) \approx 9\%$, $\mathcal{M}(R) \approx 32\%$	$\bar{a} \approx 35 \mu\text{m}$, $\bar{R} \approx 60 \mu\text{m}$ $\mathcal{M}(a) \approx 9\%$, $\mathcal{M}(R) \approx 36\%$

Table II: Averages and corresponding relative mean absolute deviations for data sets a_i and R_i in every experiment and observation. The averages \bar{a} 's are the estimates for a listed in Table I in the main text.

Since, as shown in Fig. 3, the theoretical link between ρ^* and $\lambda = a/R$ is not linear, the symmetric absolute errors $\pm\Delta\rho_i^*$ propagate asymmetrically to the corresponding a_i 's; we write them as $\pm\Delta a_i^\pm$, where

$$\Delta a_i^\pm = R_i \Delta \lambda_i^\pm + \lambda_i \Delta R \quad (\text{B2})$$

and $\Delta \lambda_i^\pm$ are defined by

$$\rho^*(\lambda_i \pm \Delta \lambda_i^\pm) = \rho_i^* \pm \Delta \rho_i^*. \quad (\text{B3})$$

Thus, we can attribute to the a_i 's the following relative error,

$$\frac{\Delta a_i}{a_i} := \frac{1}{2} \left(\frac{\Delta a_i^+}{a_i} + \frac{\Delta a_i^-}{a_i} \right) = \frac{\Delta \lambda_i}{\lambda_i} + \frac{\Delta R}{R_i}, \quad (\text{B4})$$

where $\Delta \lambda_i := (\lambda_i^+ - \lambda_i^-)/2$.

The dispersion histograms for the a_i 's and R_i 's are shown in Fig. 12 for every experiment and observation. Figure 12c is the same as Fig. 8 in the main text; it is reproduced here for completeness.

To estimate the degree of statistical dispersion for both data sets a_i 's and R_i 's, we computed the relative *mean absolute deviation* \mathcal{M} , defined for a set of n data x_i by

$$\mathcal{M}(x) := \frac{1}{\bar{x}} \frac{1}{n} \sum_{i=1}^n |x_i - \bar{x}|, \quad (\text{B5})$$

where \bar{x} denotes the (arithmetic) average of the x_i 's. A summary of the averages \bar{a} and \bar{R} , and the mean absolute deviations about them for all experiments and observations is presented in Table II. It is apparent from these data how the microcavity radii R_i are much more scattered about their averages compared to the a_i . This justifies considering the averages \bar{a} 's as estimates of a phenomenological length characteristic only of the material and its physical conditions.

-
- [1] S. V. Shiyankovskii, T. Schneider, I. I. Smalyukh, T. Ishikawa, G. D. Niehaus, K. J. Doane, C. J. Woolverton, and O. D. Lavrentovich, Real-time microbe detection based on director distortions around growing immune complexes in lyotropic chromonic liquid crystals, *Phys. Rev. E* **71**, 020702 (2005).
- [2] P. C. Mushenheim, R. R. Trivedi, H. H. Tison, D. B. Weibel, and N. L. Abbott, Dynamic self-assembly of motile bacteria in liquid crystals, *Soft Matter* **10**, 88 (2014).
- [3] P. C. Mushenheim, R. R. Trivedi, D. Weibel, and N. Abbott, Using liquid crystals to reveal how mechanical anisotropy changes interfacial behaviors of motile bacteria, *Biophys. J.* **107** **1**, 255 (2014).
- [4] S. Zhou, A. Sokolov, O. D. Lavrentovich, and I. S. Aranson, Living liquid crystals, *Proc. Natl. Acad. Sci. USA* **111**, 1265 (2014).
- [5] J. Lydon, Chromonic liquid crystal phases, *Curr. Opin. Colloid Interface Sci.* **3**, 458 (1998).
- [6] J. Lydon, Chromonics, in *Handbook of Liquid Crystals: Low Molecular Weight Liquid Crystals II*, edited by D. Demus, J. Goodby, G. W. Gray, H.-W. Spiess, and V. Vill (John Wiley & Sons, Weinheim, Germany, 1998) Chap. XVIII, pp. 981–1007.
- [7] J. Lydon, Chromonic review, *J. Mater. Chem.* **20**, 10071 (2010).
- [8] J. Lydon, Chromonic liquid crystalline phases, *Liq. Cryst.* **38**, 1663 (2011).
- [9] I. Dierking and A. Martins Figueiredo Neto, Novel trends in lyotropic liquid crystals, *Crystals* **10**, 604 (2020).
- [10] Z. S. Davidson, L. Kang, J. Jeong, T. Still, P. J. Collings, T. C. Lubensky, and A. G. Yodh, Chiral structures and defects of lyotropic chromonic liquid crystals induced by saddle-splay elasticity, *Phys. Rev. E* **91**, 050501(R) (2015), see also Erratum [42] and Supplementary Information https://journals.aps.org/pre/supplemental/10.1103/PhysRevE.91.050501/Supplementary_Info_Planar_Davidson_et_al.pdf.

- [11] J. Eun, S.-J. Kim, and J. Jeong, Effects of chiral dopants on double-twist configurations of lyotropic chromonic liquid crystals in a cylindrical cavity, *Phys. Rev. E* **100**, 012702 (2019).
- [12] J. L. Ericksen, Inequalities in liquid crystal theory, *Phys. Fluids* **9**, 1205 (1966).
- [13] S. Paparini and E. G. Virga, Paradoxes for chromonic liquid crystal droplets, *Phys. Rev. E* **106**, 044703 (2022).
- [14] L. Tortora, H.-S. Park, S.-W. Kang, V. Savaryn, S.-H. Hong, K. Kaznatcheev, D. Finotello, S. Sprunt, S. Kumar, and O. D. Lavrentovich, Self-assembly, condensation, and order in aqueous lyotropic chromonic liquid crystals crowded with additives, *Soft Matter* **6**, 4157 (2010).
- [15] L. Tortora and O. D. Lavrentovich, Chiral symmetry breaking by spatial confinement in tactoidal droplets of lyotropic chromonic liquid crystals, *Proc. Natl. Acad. Sci. USA* **108**, 5163 (2011).
- [16] C. Peng and O. D. Lavrentovich, Chirality amplification and detection by tactoids of lyotropic chromonic liquid crystals, *Soft Matter* **11**, 7221 (2015).
- [17] K. Nayani, J. Fu, R. Chang, J. O. Park, and M. Srinivasarao, Using chiral tactoids as optical probes to study the aggregation behavior of chromonics, *Proc. Natl. Acad. Sci. USA* **114**, 3826 (2017).
- [18] S. Shadpour, J. P. Vanegas, A. Nemati, and T. Hegmann, Amplification of chirality by adenosine monophosphate-capped luminescent gold nanoclusters in nematic lyotropic chromonic liquid crystal tactoids, *ACS Omega* **4**, 1662 (2019).
- [19] S. Paparini and E. G. Virga, An elastic quartic twist theory for chromonic liquid crystals, *J. Elast.* (2023).
- [20] S. Paparini and E. G. Virga, Spiralling defect cores in chromonic hedgehogs, *Liq. Cryst.* **50**, 1498 (2023).
- [21] L. Spina, M. P. De Santo, C. M. Tone, M. Pisani, F. Vita, R. Barberi, and F. Ciuchi, Intercalation or external binding: How to torque chromonic Sunset Yellow, *J. Mol. Liq.* **359**, 119265 (2022).
- [22] S. Paparini and E. G. Virga, What a twist cell experiment tells about a quartic twist theory for chromonics (2023), arXiv:2312.00149 [cond-mat.soft].
- [23] A. Pedrini and E. G. Virga, Liquid crystal distortions revealed by an octupolar tensor, *Phys. Rev. E* **101**, 012703 (2020).
- [24] J. V. Selinger, Director deformations, geometric frustration, and modulated phases in liquid crystals, *Ann. Rev. Condens. Matter Phys.* **13**, 49 (2022).
- [25] C. Long and J. V. Selinger, Explicit demonstration of geometric frustration in chiral liquid crystals, *Soft Matter* **19**, 519 (2023).
- [26] E. G. Virga, Uniform distortions and generalized elasticity of liquid crystals, *Phys. Rev. E* **100**, 052701 (2019).
- [27] S. Paparini and E. G. Virga, Stability against the odds: the case of chromonic liquid crystals, *J. Nonlinear Sci.* **32**, 74 (2022).
- [28] C. W. Oseen, The theory of liquid crystals, *Trans. Faraday Soc.* **29**, 883 (1933).
- [29] F. C. Frank, On the theory of liquid crystals, *Discuss. Faraday Soc.* **25**, 19 (1958).
- [30] O. D. Lavrentovich and E. M. Terent'ev, Phase transition altering the symmetry of topological point defects (hedgehogs) in a nematic liquid crystal, *Sov. Phys. JETP* **64**, 1237 (1986), Translated from: *Zh. Eksp. Teor. Fiz.* **91**(6), 2084–2086 (December 1986). <http://www.jetp.ras.ru/cgi-bin/e/index/e/64/6/p1237?a=list>.
- [31] R. Cohen and M. Taylor, Weak stability of the map $x/|x|$ for liquid crystal functionals, *Comm. PDE* **15**, 675 (1990).
- [32] D. Kinderlehrer and B. Ou, Second variation of liquid crystal energy at $x/|x|$, *Proc. R. Soc. Lond. A* **437**, 475 (1992).
- [33] A. Rudinger and H. Stark, Twist transition in nematic droplets: a stability analysis, *Liq. Cryst.* **26**, 753 (1999).
- [34] P. Bao, D. A. Paterson, S. A. Peyman, J. C. Jones, J. A. T. Sandoe, H. F. Gleeson, S. D. Evans, and R. J. Bushby, Production of giant unilamellar vesicles and encapsulation of lyotropic nematic liquid crystals, *Soft Matter* **17**, 2234 (2021).
- [35] S. Zhou, Y. A. Nastishin, M. M. Omelchenko, L. Tortora, V. G. Nazarenko, O. P. Boiko, T. Ostapenko, T. Hu, C. C. Almasan, S. N. Sprunt, J. T. Gleeson, and O. D. Lavrentovich, Elasticity of lyotropic chromonic liquid crystals probed by director reorientation in a magnetic field, *Phys. Rev. Lett.* **109**, 037801 (2012).
- [36] S. Zhou, K. Neupane, Y. A. Nastishin, A. R. Baldwin, S. V. Shiyankovskii, O. D. Lavrentovich, and S. Sprunt, Elasticity, viscosity, and orientational fluctuations of a lyotropic chromonic nematic liquid crystal disodium cromoglycate, *Soft Matter* **10**, 6571 (2014).
- [37] S. Zhou, Recent progresses in lyotropic chromonic liquid crystal research: elasticity, viscosity, defect structures, and living liquid crystals, *Liq. Cryst.* **27**, 91 (2018).
- [38] V. G. Taratuta, F. Lonberg, and R. B. Meyer, Anisotropic mechanical properties of a polymer nematic liquid crystal, *Phys. Rev. A* **37**, 1831 (1988).
- [39] T. Odijk, Elastic constants of nematic solutions of rod-like and semi-flexible polymers, *Liq. Cryst.* **1**, 553 (1986).
- [40] V. M. Pergamenschik, Kinetic energy of flexible aggregates and universal power-law behavior of self-assembling in a thermal bath, *Eur. Phys. J. Spec. Top.* **216**, 219 (2013).
- [41] V. M. Pergamenschik and A. B. Vozniak, Statistical model of a flexible inextensible polymer chain: The effect of kinetic energy, *Phys. Rev. E* **95**, 012501 (2017).
- [42] Z. S. Davidson, L. Kang, J. Jeong, T. Still, P. J. Collings, T. C. Lubensky, and A. G. Yodh, Erratum: Chiral structures and defects of lyotropic chromonic liquid crystals induced by saddle-splay elasticity [*Phys. Rev. E* 91, 050501(R) (2015)], *Phys. Rev. E* **92**, 019905 (2015).